U.S. DEPARTMENT OF ENERGY | Office of Science

DOE/SC-ARM-15-074

Shortwave Hyperspectral Observations During MAGIC Final Campaign Summary

PJ McBride
A Marshak
W Yang

March 2016

ARM
CLIMATE RESEARCH FACILITY

DISCLAIMER

DOE/SC-ARM-15-074

Shortwave Hyperspectral Observations During MAGIC Final Campaign Summary

PJ McBride, Atmospheric & Space Technology Research Associates
W Yang, Goddard Space Flight Center
A Marshak, Goddard Space Flight Center
Principal Investigators

March 2016

Work supported by the U.S. Department of Energy,
Office of Science, Office of Biological and Environmental Research

Acronyms and Abbreviations

ARM	Atmospheric Radiation Measurement
Cimel	Cimel sunphotometer
GEWEX	Global Energy and Water Cycle Exchanges (project)
GCSS	GEWEX Cloud Systems Study
GPCI	GCSS Pacific Cross-Section Intercomparison
HSRL	high spectral resolution lidar
MAGIC	Marine ARM GPCI Investigation of Clouds
NASA	National Aeronautics and Space Administration
SAS-Ze	shortwave array spectrometer
SBDART	Santa Barbara Discrete Atmospheric Radiative Transfer (model)
SSFR	solar spectral flux radiometer
TSI	total sky imager

Contents

Acronyms and Abbreviations iii
1.0 Background 1
2.0 Notable Events or Highlights 1
3.0 Lessons Learned 1
4.0 Results 1
4.1 Instrument Comparisons 1
4.2 Observations of Cloudy Transition Zones Using SSFR and SAS_Ze 4
4.2.1 Simulation over Oceanic Tropical Areas 4
4.2.2 Relations between Variations of Intercept and Cloud Particle Size 6
4.3 Observations of Cloudy Transition Zones Using SSFR and SAS_Ze 6
5.0 Marine ARM GPCI Investigation of Clouds Publications 10
5.1 Journal Articles/Manuscripts 10
5.2 Meeting Abstracts/Presentations/Posters 10
6.0 References 11

Figures

1. Comparison of the SAS-Ze, Cimel sunphotometer, and SSFR shown as a percent difference from the Cimel instrument. This comparison is based on measurements taken during three cloudy cases over the course of July 2013 (Yang et al. 2014). *Left:* Deviations of SSFR and SAS_Ze from the Cimel instrument. *Right:* Deviations between SSFR and SAS_Ze. 2
2. Time series of the slope and y-intercept of a line fit to the normalized radiance from SSFR (red) and SAS-Ze (yellow) for MAGIC data taken on July 8, 2013 (Yang et al. 2014) 3
3. Comparisons of the self-normalized radiances among instruments using the same data as in Figure 1. *Left:* Deviation of SSFR and SAS_Ze from the Cimel sunphotometer in the normalized radiance values. *Right:* Deviation of SSFR from SAS_Ze in the normalized radiance values. Compared to Figure 1, the deviations of self-normalized radiances among instruments are much smaller. 4
4. Left: slope of the regression line fit over the *ratio-to-clear* versus *cloudy-to-clear* ratio for the spectral range between 400 and 870 nm. Right: Slope of the regression line fit over the *ratio-to-clear* versus *cloudy-to-clear* ratio for the spectral range between 1530 nm and 1660 nm. The black contours show percent cloud absorption at 1600 nm calculated with SBDART. These calculations were done with a known clear $\tau = 0$ and $\mu = 0.7$ where μ is the cosine of the solar zenith angle. 5
5. HSRL LIDAR backscatter cross-section profiles during cloudy-to-clear sky transitions July 10, 2013 (left) and July 12, 2013 (right). Total sky images also are shown. 7
6. Time series of observations. (a)-(d) zenith radiance at 500 nm, ratio R(870/440), slope of visible band and intercept of near-infrared band in the case of July 10, 2013; (e)-(h) zenith radiance at 500 nm, ratio R(870/440), slope of visible band and intercept of near-infrared band in the case of July 12, 2013. 8

1.0 Background

The Marine ARM GPCI[1] Investigation of Clouds (MAGIC) field campaign was initiated to improve our understanding of low-level marine clouds that have a significant influence on the Earth's climate. The campaign was conducted using an ARM mobile facility deployed on a commercial ship traveling between Honolulu, Hawaii, and Los Angeles, California, from October 2012 to September 2013. The solar spectral flux radiometer (SSFR) was deployed on July 6, 2013, through the end of the campaign. The SSFR was calibrated and installed by Warren Gore of NASA Ames Research Center, and the data is and will be analyzed by Drs. Alexander Marshak and Weidong Yang of NASA Goddard Space Flight Center, Dr. Samuel LeBlanc of NASA Ames Research Center, Dr. Sebastian Schmidt of the University of Colorado-Boulder, and Dr. Patrick McBride of Atmospheric & Space Technology Research Associates in Boulder, Colorado.

2.0 Notable Events or Highlights

The quantity and variety of the surface-based observations of marine clouds make the MAGIC data interesting as a whole. The SSFR provides hyperspectral observations in the visible and near-infrared regions that allow for cloud property retrievals. In addition, its data can be used to make surface energy budget calculations in oceanic regions where surface-based observations present obvious challenges.

3.0 Lessons Learned

Calibrating frequently during future ship-based campaigns could be beneficial. Typically, the SSFR is deployed on aircraft rather than on ships, with calibrations occurring after each flight. While the change in the SSFR response is typically very stable, on the order of 1 to 2% over a month-long campaign, regular monitoring of the response over the length of a campaign provides more confidence in the results and can help explain differences that arise when comparing observations of other instruments.

4.0 Results

4.1 Instrument Comparisons

The period of deployment of the SSFR overlapped with two other zenith pointing instruments, the Cimel sunphotometer operating in cloud mode and the shortwave array spectrometer (SAS-Ze). Both of these instruments have some spectral overlap with the SSFR, thus allowing comparisons of observations taken from different parts of the ship by the three instruments. These comparisons illustrated inconsistencies in the absolute calibrations of the instruments. The SAS-Ze and SSFR exhibited approximately 20% differences for three cloudy cases analyzed during July 2013 (see Figure 1). When compared to the Cimel sunphotometer on these same three days, the SSFR and SAS_Ze instruments differed consistently on July 6 and July 9. The difference between measurements made by the SAS_Ze and Cimel instruments was approximately -20%, and the difference between the SSFR-Cimel instruments was approximately 10%. Differences between measurements taken on July 18 were quite different. The differences between

[1]GPCI = GCSS Pacific Cross-section Intercomparison, a working group of GCSS
GCSS = GEWEX Cloud Systems Study
GEWEX = Global Energy and Water Cycle Experiment, a core project of the World Climate Research Programme.

measurements taken by the SAS_Ze-Cimel instruments and the SSFR-Cimel instruments both increased by approximately 40% as shown in Figure 1.

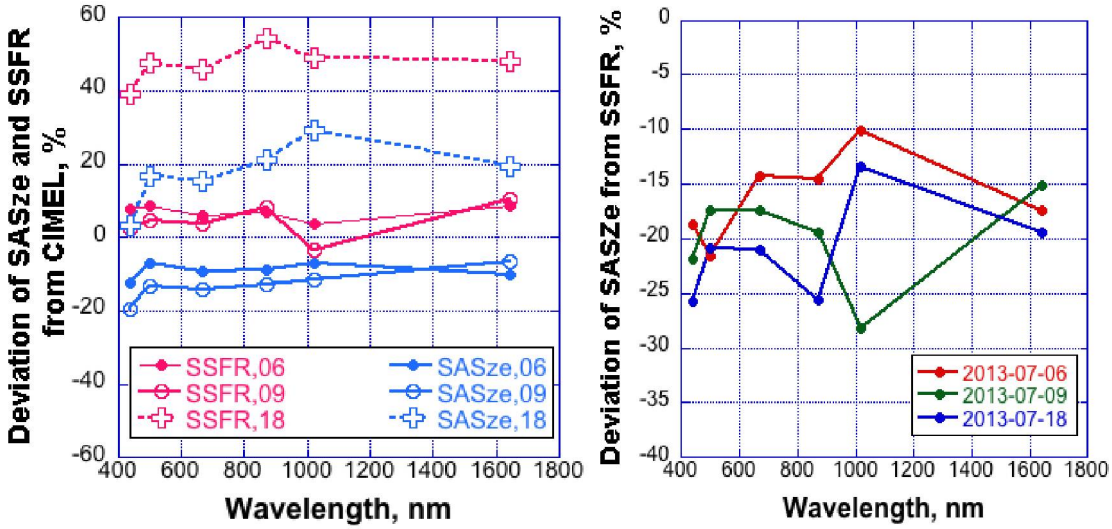

Figure 1. Comparison of the SAS-Ze, Cimel sunphotometer, and SSFR shown as a percent difference from the Cimel instrument. This comparison is based on measurements taken during three cloudy cases over the course of July 2013 (Yang et al. 2014). *Left:* Deviations of SSFR and SAS_Ze from the Cimel instrument. *Right:* Deviations between SSFR and SAS_Ze.

The comparisons of the two hyperspectral instruments, the SSFR and SAS-Ze, show significant differences in their absolute calibration, but correlate reasonably well in the relative sense. An algorithm developed for application in the cloud transition zone (Chiu et al. 2010) uses the slope and y-intercept of a line fit to surface-based radiance measurements normalized by a radiance observations taken at a single wavelength. This technique reduces the dependence on the absolute calibration. The graphs in Figure 2, which is taken from Yang et al. (2014), show that the line parameters, slope, and intercept are virtually identical when the normalized radiances are used from both the SAS-Ze and the SSFR.

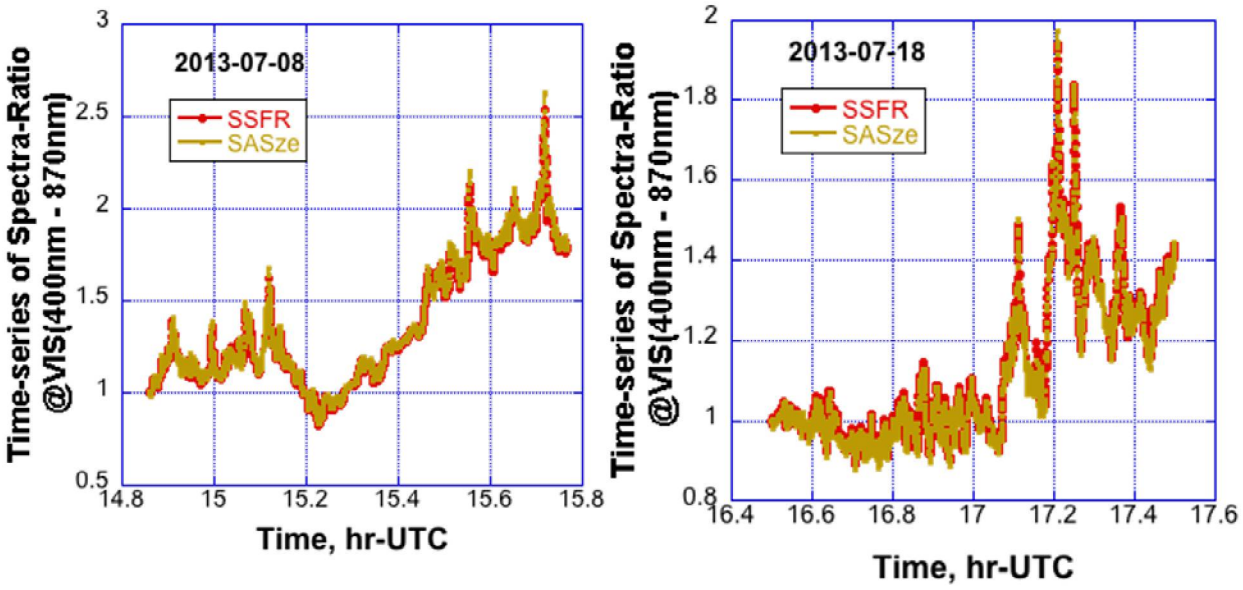

Figure 2. Time series of the slope and y-intercept of a line fit to the normalized radiance from SSFR (red) and SAS-Ze (yellow) for MAGIC data taken on July 8, 2013 (Yang et al. 2014).

Further comparisons of the self-normalized radiances between instruments show that normalized values are quite consistent and deviations are much smaller among instruments. The self-normalized radiance is defined as $R'\lambda(t) = R\lambda(t)/R\lambda(t0)$, where R and R' denote the radiance and normalized radiance at wavelength λ, and t and t0 are the time being investigated and the initial time of the time series, respectively.

Figure 3(a) shows that the differences in the self-normalized radiances between instruments on the same three days are reduced when compared to the differences in the absolute radiances (~20%) shown in Figure 1 (right image).

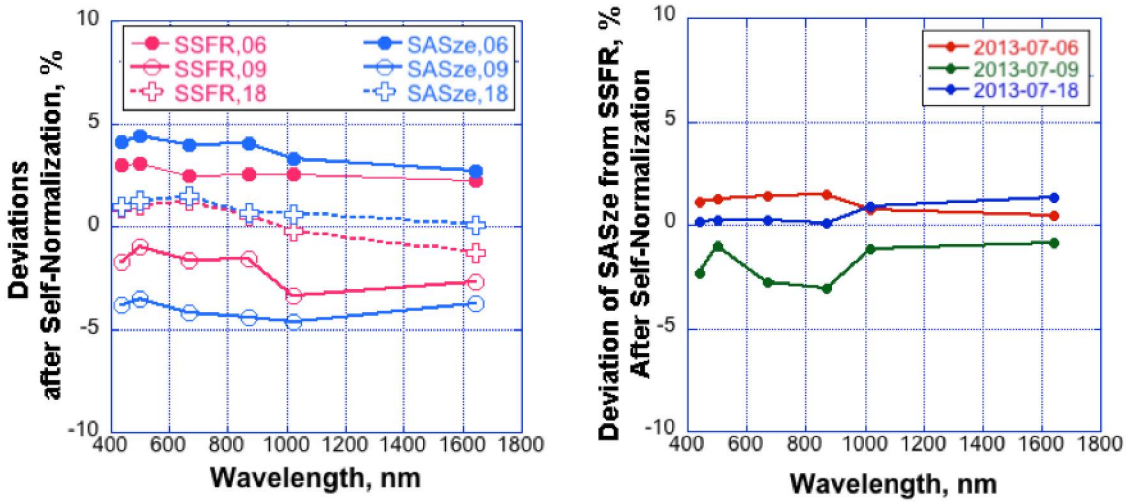

Figure 3. Comparisons of the self-normalized radiances among instruments using the same data as in Figure 1. *Left:* Deviation of SSFR and SAS_Ze from the Cimel sunphotometer in the normalized radiance values. *Right:* Deviation of SSFR from SAS_Ze in the normalized radiance values. Compared to Figure 1, the deviations of self-normalized radiances among instruments are much smaller.

4.2 Observations of Cloudy Transition Zones Using SSFR and SAS_Ze

The time-resolved hyperspectral measurements from SSFR and SAS_Ze during MAGIC provide a unique opportunity to study cloud properties such as optical thickness τ and effective radius r_{eff} in the transition zone between cloudy and clear skies. Motivated by earlier discoveries on relationships between cloud spectral invariances and cloud optical properties, we studied the spectral-invariant properties of two transition zones observed on July 10 and July 12, 2013.

Spectrally invariant properties are characterized by a linear relationship between the slope and intercept, whereby spectra in the cloud transition zone can be approximated as a linear combination of definitely clear and cloudy spectra. Our understanding of the variations of the spectral invariances is based on analysis of simulation results from a simple SBDART model that contains only one layer of low clouds over tropical oceanic areas.

4.2.1 Simulation over Oceanic Tropical Areas

To investigate how the spectral invariance properties vary with the optical thickness and effective radius, spectral invariance calculations based on the SBDART model are performed using values of τ between 0.1 and 5 at steps of 0.1 and values of r_{eff} between 4 and 16 μm at steps of 0.1 μm. The left panel of Figure 4 shows that $slope_{vis}$, and its dependence on the optical thickness, is clear even for these optically thin clouds.

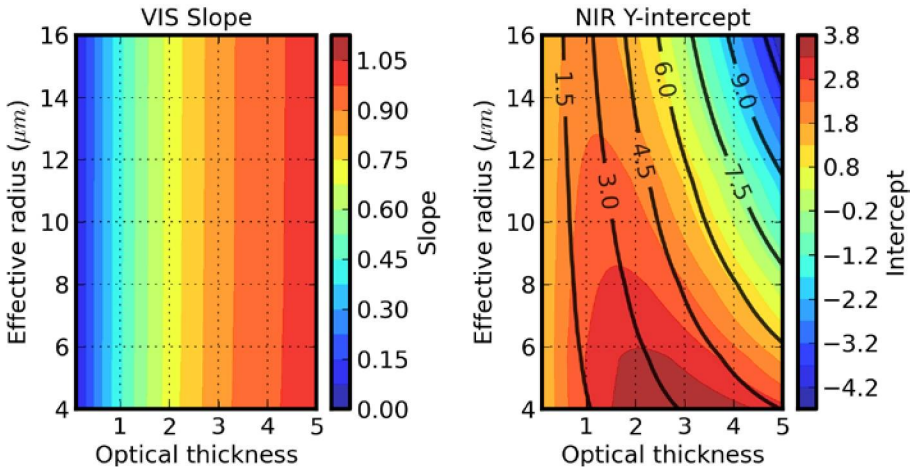

Figure 4. Left: slope of the regression line fit over the *ratio-to-clear* versus *cloudy-to-clear* ratio for the spectral range between 400 and 870 nm. Right: Slope of the regression line fit over the *ratio-to-clear* versus *cloudy-to-clear* ratio for the spectral range between 1530 nm and 1660 nm. The black contours show percent cloud absorption at 1600 nm calculated with SBDART. These calculations were done with a known clear $\tau = 0$ and $\mu = 0.7$ where μ is the cosine of the solar zenith angle.

As optical thickness decreases, $slope_{vis}$ decreases with almost no dependence on $r_{eff.}$ The right panel of Figure 4 shows int_{nir} in the colored contours with the cloud absorption at 1600 nm overlaid with black contours. The cloud absorption contours, calculated as a percentage of the top-of-atmosphere irradiance, help explain the shape of the int_{nir} contours. For the strongest absorption (>4.5% shown here), int_{nir} and cloud absorption are well correlated and the dependence of int_{nir} on r_{eff} is strongest. For absorption between 1.5 and 4.5%, the dependence on r_{eff} and the correlation with absorption lessens, and below the 1.5% absorption contour ($\tau \leq 1$), there is almost no size dependence due to insufficient liquid water absorption. Clearly, in the cloud transition zone analysis, decreasing $slope_{vis}$ can be used to indicate (in)decreasing optical thickness as the scene transitions from cloudy to cloudless skies while int_{nir} can be used to determine the relative changes in r_{eff} with an (de)increasing int_{nir} indicating a (in)decreasing $r_{eff.}$

Throughout the research, the notion of known cloudy and known clear observations has been used. Determining the cloud properties of optically thin clouds is highly uncertain, and for very thin clouds, even making a cloud/no cloud decision can be difficult. Given the challenges of ensuring a completely cloudless sky, it is important to explore the impacts of cloud contamination in the known clear observation. The calculations upon which Figure 4 is based have been repeated with the known clear spectrum ($\tau = 0$) replaced by a spectrum modeled with a τ of 0.1 and r_{eff} of 8 μm. The resulting look-up table (not shown here) shows changes in the values of the slope and intercept, but the contour shapes are relatively unchanged.

The zenith radiance and hence the slope and intercept of the spectrally invariant-based technique depend on the solar zenith angle. All of the previous model calculations were done with a $\mu = 0.7$. The effect of solar zenith angle can be tested by simply repeating the calculations using different values for μ. The test results for $\mu = 0.3$ show that changes in the solar geometry may affect the values of the slope and intercept, but these changes are small and limited.

4.2.2 Relations between Variations of Intercept and Cloud Particle Size

The previously discussed calculation uses simple models to demonstrate the dependence of spectral invariance on cloud optical thickness and effective size including the effects of solar angle and cloud contaminations. Joint application of the panels of Figure 4 can potentially allow the cloud optical thickness and particle size to be retrieved if the initial known cloud optical thickness is known. Indeed, a full quantitative and precise study also requires comprehensive models that include the aerosol properties, cloud geometries, etc. However, the results from the simplified model (upon which Figure 4 is based) would reflect the major features and are ready to help us predict the qualitative information of variations of clouds particle size without the knowledge of the known cloud optical thickness.

Figure 4 shows that, at larger optical thickness, int_{nir} and r_{eff} are negatively correlated; however, at a low optical thickness of $\tau \leq 1$), there is little sensitivity to r_{eff}, and there are regions where dual solutions exist. Dual solutions are cases in which a change in r_{eff} can result from both an increasing and decreasing int_{nir}. To quantify the ability of int_{nir} to correctly predict the relative change in r_{eff}, simulations were run for 10^5 cases. Each case consisted of two randomly chosen τ- r_{eff} pairs in the range of Figure 4. The two points were ordered so that τ was decreasing to match the assumption in the cloud transition zone. Cases where r_{eff} and int_{nir} were negatively correlated were counted as a success. We found that int_{nir} was able to predict the change in droplet size in 74% of the 10^5 cases for the model as shown in Figure 4, the same 74% for considering the cloud contamination case, and 73% to 77% for various solar zenith angles.

These large successful rates mean that, without having additional information, the intercept of regression lines in the near-infrared region can be used as a good indicator of cloud droplet size in the transition zone: increasing (decreasing) intercepts likely indicate decreasing (increasing) cloud droplet sizes.

4.3 Observations of Cloudy Transition Zones Using SSFR and SAS_Ze

Two cloud transition zone cases are discussed in this study. The observations of the two cases and their corresponding spectral-invariant properties are shown in Figure 5 and Figure 6. These two cases show transitions from cloud to aerosol skies and are around 01:13 UTC on July 10, 2013 (left) and 00:57 UTC on July 12, 2013 (right). The backscatter profiles of high spectral resolution lidar (HSRL) as well as the total sky imager (TSI) images in Figure 5, show that clouds in the transition zones were low clouds at altitude of approximately 1.4 km and 0.8 km, respectively. These cases consisted of liquid water clouds that were not producing drizzle. Therefore, the cloudy sky properties in both cases were dominated by the water clouds (instead of ice crystals); thus they are suitable for the studies reported in this document.

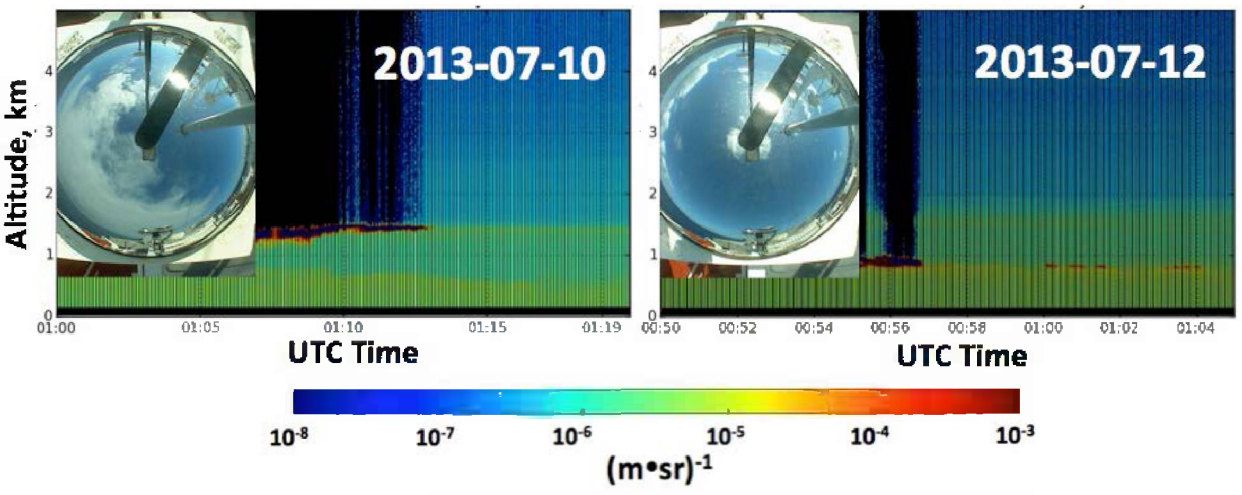

Figure 5. HSRL LIDAR backscatter cross-section profiles during cloudy-to-clear sky transitions July 10, 2013 (left) and July 12, 2013 (right). Total sky images also are shown.

The radiance measurements and the spectrally invariant slopes and intercepts of the case on July 10, 2013, are shown in Figure 6(a) through (d), while those of July 12, 2013, are shown in Figure 6(e) through (h).

On July 10, 2013, the zenith radiances at 500 nm gradually decreased from around 140 to 40 (W*m-2m-2sr-1) from both instruments (Figure 6(a)). Because scattering in clear skies originates mostly from molecular and aerosol scattering, the zenith radiances at 500 nm under clear skies are much smaller than those of cloudy skies (if the cloud is not optically thick). The high dynamic range of the radiance measurements indicates that this time period transitions from obvious cloudy skies to clear skies. Specifically, based on SSFR measurements, the obvious clear skies start around 1.215 UTC hour, while based on SAS_Ze and Cimel sunphotometer measurements, clear skies start around 1.2125 UTC hour. Figure 6(b) shows the time series of the ratios of normalized radiances of 870 nm over 440 nm (R(870/440)) where the radiances are normalized to solar radiances at the top of atmosphere.

Aerosol particles are small and scatter more light at shorter wavelength than at longer wavelength, while cloud particles are larger and have about the same scattering ability at both shorter and longer wavelengths. These characteristics result in ratios near 1 for clouds and much smaller ratios than 1 for clear sky. However, over the time shown, the ratio R(870/440) (as well as the radiance shown in Figure 6(a)) varies continuously and decreases gradually with time. For the sake of discussion, we divided the whole transition time into three sub-regions. If we define R(870/440) >0.8 as an indicator of an obvious cloudy sky here, Figure 6(b) depicts an obvious cloudy sub-region up to 1.208 UTC hour where R(870/440) decreases from ~1.2 to ~0.8, followed by an ambiguous sub-region where R(870/440) decreases from ~0.8 to ~0.2, and then an obvious clear sky sub-region with R(870/440) less than approximately 0.2. Defining obvious cloudy skies as R(870/440) >0.8 is somewhat arbitrary. However, this value can indicate that the cloud optical properties have been affected significantly by those of clear skies. Therefore, this value is kept as the criteria of obvious clouds in this report.

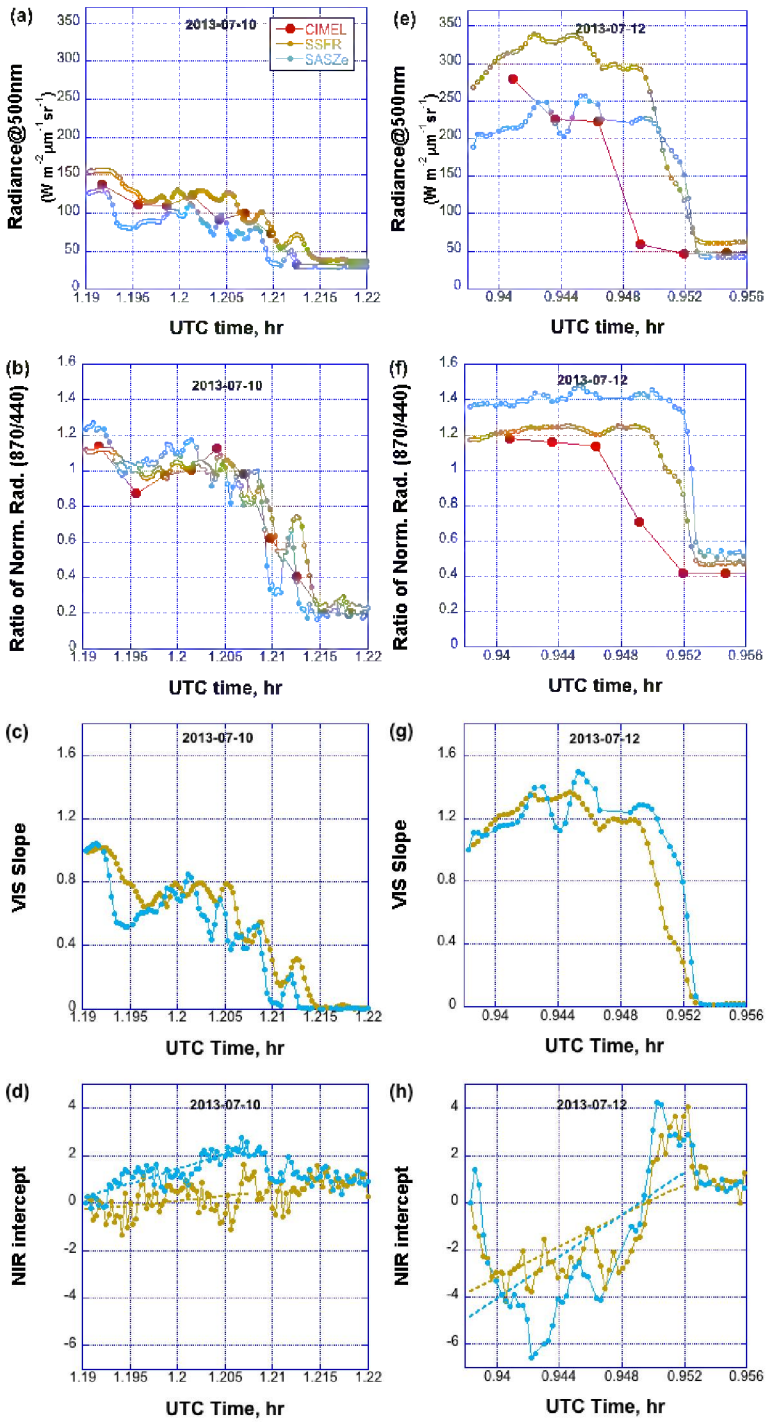

Figure 6. Time series of observations. (a)-(d) zenith radiance at 500 nm, ratio R(870/440), slope of visible band and intercept of near-infrared band in the case of July 10, 2013; (e)-(h) zenith radiance at 500 nm, ratio R(870/440), slope of visible band and intercept of near-infrared band in the case of July 12, 2013.

Spectra were taken at 1.19 UTC hour and at 1.22 UTC hour as the known cloudy sky and known clear sky, respectively, to calculate the slopes of visible band and the intercepts of the infrared band. The

results from the SSFR and SAS_Ze are shown in Figure 6(c) through (d). In the obvious cloudy sub-region, both instruments demonstrate a decreasing trend in slopes and increasing trend in intercepts as the edge of obvious cloud is approached, though fluctuations exist on finer time scales. The decreasing slopes mean the optical thickness of the cloud is decreasing, while the increasing intercepts indicate that the cloud particle size is likely decreasing at the cloud edge (see Section 4.2.). In the ambiguous sub-region, from 1.208UTC hour to 1.215 UTC hour, the same trends in slope but opposite trends in intercept are observed from the two instruments. The decreasing slope can still be understood as the result of decreasing optical thickness of clouds in this sub-region. However, the intercepts in this sub-region could result from noise because cloud optical thickness in this region likely is very thin and the intercepts are not responsive to the changes in cloud particle size (see Section. 4.2). In the sub-region of obvious clear sky after 1.215 UTC hour, both the slope and intercept are stabilized around 0 and 1, respectively, from both instruments. This is an indication of clear sky in the spectrally invariant properties.

In the July 12 case, the time series of zenith radiances shows a transition from a much higher value of ~250 to a lower value of ~50 (Figure 6(e)). This shows an obvious clear sky starting from ~0.953 UTC hour for the SSFR and SAS_Ze and from ~0.952 UTC hour for the Cimel. In addition, the ratio R(870/440) transitions from ~1.3 to ~0.5 during the same time period (Figure 6(f)), though this ratio differs among the three instruments. By using the same ratio (>0.8) to define obvious cloudy skies as in the July 10 case, Figure 6(f) shows obvious cloudy skies before ~0.9525 UTC hour for measurements from SSFR and SAS_Ze and before ~0.9485 UTC hour for measurements from the Cimel. Figure 6(g) through (h) illustrate the evolution of the spectrally invariant properties for the July 12 case from SSFR and SAS_Ze measurements. Similar to the July 10 case, the slopes of visible band decrease when the edge of obvious cloudy sub-region is approached (Figure 6(g)), indicating a decrease in the cloud optical thickness. The slope, and therefore the cloud optical thickness, continues to decrease in the ambiguous sub-region until the start of the obvious clear sub-region. These trends in the slope are consistent with the trends of radiance measurements and ratios R(870/440) shown in Figure 6(e) through (f), where decreasing values also are observed over time. Also, as in the July 10 case, the intercepts of infrared bands in the obvious cloudy sub-region show an increasing trend before the end of the time sub-region. This indicates that the cloud particle size also is likely decreasing when the cloud edge is approached. In the succeeding ambiguous sub-region, the intercept decreases to a value ~1 for the obvious clear sky sub-region.

The two case studies presented here show significant differences aside from the similarities previously discussed. First, the zenith radiance values in the obvious cloudy and obvious clear skies of July 12 are about twice as large as the values of July 10. Second, the ambiguous sub-region of the July10 case lasted ~25 seconds while the July 12 case lasted ~2 to ~3 seconds for the SSFR and SAS_Ze instruments. (Note that the temporal resolution of the Cimel instrument is about ten seconds; therefore, the ambiguous sub-region from Cimel measurements looks much longer than it should be). The speed of the cloud relative to the ship speed in the July 12 case was approximately twice that of the July 10 case (estimated by observing the TSI images). The transition on July 12 was still much more rapid than on July 10. Because the cloud speed on July 12 was ~10 m/s (approximated by observing the TSI images and the cloud height from HSRL), we determined the size of the ambiguous sub-region on July 10 to be ~125 m, while on July 12, it was ~20 to ~30 m. These differences are likely related to the cloud types that can be seen in the spatial distribution seen in the TSI images and HSRL profiles of Figure 5. The clouds on July 10 were thinner and more widely spread than on July 12.

Note that in this report the transitions from cloudy to clear skies are divided into three sub-regions according to the values of radiance measurements and the ratio R(870/440). In fact, the definition of boundaries of these sub-regions can be problematic because of the continuum nature of the transitions. However, the three sub-regions defined in this report reflect the basic characteristics of the evolution of cloud properties during the transitions and provide convenience for understanding and discussion.

The comparisons described above clearly show that, when the cloud edges are approached during the transition, measurements from both SSFR and SAS_Ze instruments demonstrate a decreasing trend in the slope of the visible band and an increasing trend in the intercept of the near-infrared band. Based on the results of simulations described in Section 4.2, this indicates that, when the cloud edges are approached during the transition, the cloud optical thickness decreases and the cloud particle effective size likely decreases in both of these cases. We note that the time series of LIDAR vertical profiles can be used to find the shapes of cloud vertical cross sections during the transitions. We found that neither of the two cases is from a cloud with a dome-shaped top and a flat base, where the averaged altitude of cloud edges is much lower than the inner part far from cloud edges. Because the cloud particle size is positively related to altitude, the average cloud particle size near the edge of a dome-shaped cloud is expected to be smaller than particles found far from the edges. Therefore, in the two cases studied, the decreasing cloud optical thickness and decreasing particle size near cloud edges reflect the physical processes rather than merely the natural effects of altitude changes of clouds.

5.0 Marine ARM GPCI Investigation of Clouds Publications

5.1 Journal Articles/Manuscripts

W. Yang et al. *Observation of the spectral-invariant properties of clouds during cloudy-to-clear transition in MAGIC, A case study.* In preparation.

5.2 Meeting Abstracts/Presentations/Posters

Marshak A, PJ McBride, C Chiu, and WJ Wiscombe. 2014. "MAGIC hyperspectral observations for studying cloud properties." MAGIC Science Workshop, May 5-7, 2014, Brookhaven National Laboratory, Upton, New York.

McBride PJ, A Marshak, S Schmidt, WJ Wiscombe. 2013. "Properties of clouds and the cloud transition zone retrieved from ship-borne hyperspectral observations during MAGIC." Poster presented at American Geophysical Union Fall Meeting, December 9-13, 2013, San Francisco, California.

McBride PJ and A Marshak. 2014. "Studying cloud droplet variability in the cloud transition zone using surface-based hyperspectral observations." Poster presented at American Meteorological Society 14th Conference on Atmospheric Radiation, July 7-11, 2014, Boston, Massachusetts.

Yang W, A Marshak, PJ McBride, C Flynn, S Schmidt, C Chiu, and E Lewis. 2015. Analysis of shortwave spectrometry of cloudy atmospheres during MAGIC. Presented at the ARM/ASR Joint User Facility and Principal Investigator Meeting, March 15-20, 2015, Vienna, Virginia.

6.0 References

Chiu, JC, A Marshak, Y Knyazikhin, and WJ Wiscombe. 2010. "Spectrally-invariant behavior of zenith radiance around cloud edges simulated by radiative transfer." *Atmospheric Chemistry and Physics* 10(22):11295-11303. doi:10.5194/acp-10-11295-2010, 2010.

www.arm.gov

U.S. DEPARTMENT OF
ENERGY

Office of Science